

Bichromatic Quantum Teleportation of Weak Coherent Polarization States on a Metropolitan Fiber

Zofia A. Borowska¹, Shane Andrewski², Giorgio De Pascalis³, Olivia Brasher², Mael Flament², Alexander N. Craddock², Niccolò Bigagli², Ronny Döring¹, Michaela Ritter¹, Ralf-Peter Braun⁴, Klaus Jons³, Marc Geitz¹, Oliver Holschke¹, Matheus Sena¹, and Mehdi Namazi²

¹Deutsche Telekom AG, Winterfeldtstraße 21, 10781 Berlin, Germany

²Qunnect Inc, 141 Flushing Ave, Suite 1110, Brooklyn, NY 11205, USA

³Institute for Photonic Quantum Systems (PhoQS),

Center for Optoelectronics and Photonics Paderborn (CeOPP) and Department of Physics, Paderborn University, Warburgerstraße 100, 33098 Paderborn, Germany and

⁴Orbit GmbH, Mildret-Scheel-Straße 1, 53175 Bonn, Germany

(Dated: February 19, 2026)

As quantum technologies mature, telecommunication operators have a clear opportunity to unlock and scale new services by providing the connectivity layer that links quantum computers, sensors, clocks, and other quantum devices. Realizing this opportunity requires demonstrating quantum networking protocols, including quantum teleportation, under real-world conditions on existing telecom infrastructure. In this work, we demonstrate quantum teleportation over Deutsche Telekom's metropolitan fiber testbed in Berlin using commercial components deployed at the telecom datacenter. A local Bell-state measurement between 795 nm photons from a weak coherent source and from a bichromatic warm-atom entangled photon source enables conditional state transfer onto an O-band photon, which is transmitted through a 30-km field-deployed fiber loop under real-world environmental conditions. The teleported state is reconstructed after propagation via state tomography, achieving an average teleportation fidelity of 90% on the deployed link. System performance is evaluated in both the absence and the presence of co-propagating C-band classical traffic within the same fiber, demonstrating compatibility with wavelength-division multiplexed telecom infrastructure carrying live data channels.

I. INTRODUCTION

Quantum teleportation [1] is a fundamental primitive for quantum networking [2] utilizing shared entanglement to transfer an unknown qubit state from a sender to a remote receiver. Teleportation underpins distributed quantum computing [3], remote quantum sensing and processing [4], and, when combined with entanglement swapping, quantum-repeater architectures that extend the reach of the network [5].

For teleportation and related quantum networking protocols, practical deployment requires robust operation in real-world optical fiber networks. In such environments, quantum signals must coexist with classical wavelength-division multiplexed (WDM) channels that carry conventional traffic [6], allowing efficient use of existing infrastructure and commercially available components. Operating under these conditions introduces additional physical-layer impairments. In particular, polarization-entanglement-based protocols (well suited for interfacing with matter qubits such as trapped ions and neutral atoms) are highly sensitive to time-varying fiber birefringence, which induces polarization drifts [7]. Moreover, when quantum signals share the fiber with co-propagating classical traffic, inter-channel crosstalk introduces excess noise, degrading the quality of distributed entanglement regardless of the photonic encoding (e.g., polarization [8] or energy-time [9]). Stable operation therefore relies on two key techniques. Automatic polarization compensation mitigates envi-

ronmentally induced polarization rotations [10], while wavelength-division multiplexing provides spectral separation between quantum and classical signals, creating a spectral guard band that suppresses classical noise and preserves entanglement fidelity.

In previous work [11], we introduced the *BearlinQ* testbed and demonstrated high-fidelity entanglement distribution over a live field-deployed optical network. Fidelities between 85% and 99% were achieved with less than 1.5% network downtime, and stable long-term operation was maintained over distances up to 100 km. Building on this foundation, a natural next step is to demonstrate quantum teleportation on the same infrastructure, whilst distributing the entanglement through the live carrier-grade metropolitan network. Demonstrating this constitutes a milestone toward scalable quantum networking and provides evidence of telecom-operator-run quantum teleportation. Furthermore, a practical quantum internet will also be intrinsically heterogeneous. Many platforms naturally couple to photons near atomic transitions, such as atomic systems operating at 780-795 nm, whereas low-loss transmission in deployed fiber is optimal in the telecom O/C-bands. Teleportation supported by a bichromatic entanglement source can enable wavelength bridging by mapping a device-compatible photonic qubit at 780-795 nm onto a fiber-compatible telecom photon via a Bell-state measurement. Scaling beyond a single span then requires telecom-band entanglement swapping between links [12] but here, we instead focus on the complementary end-node function: the

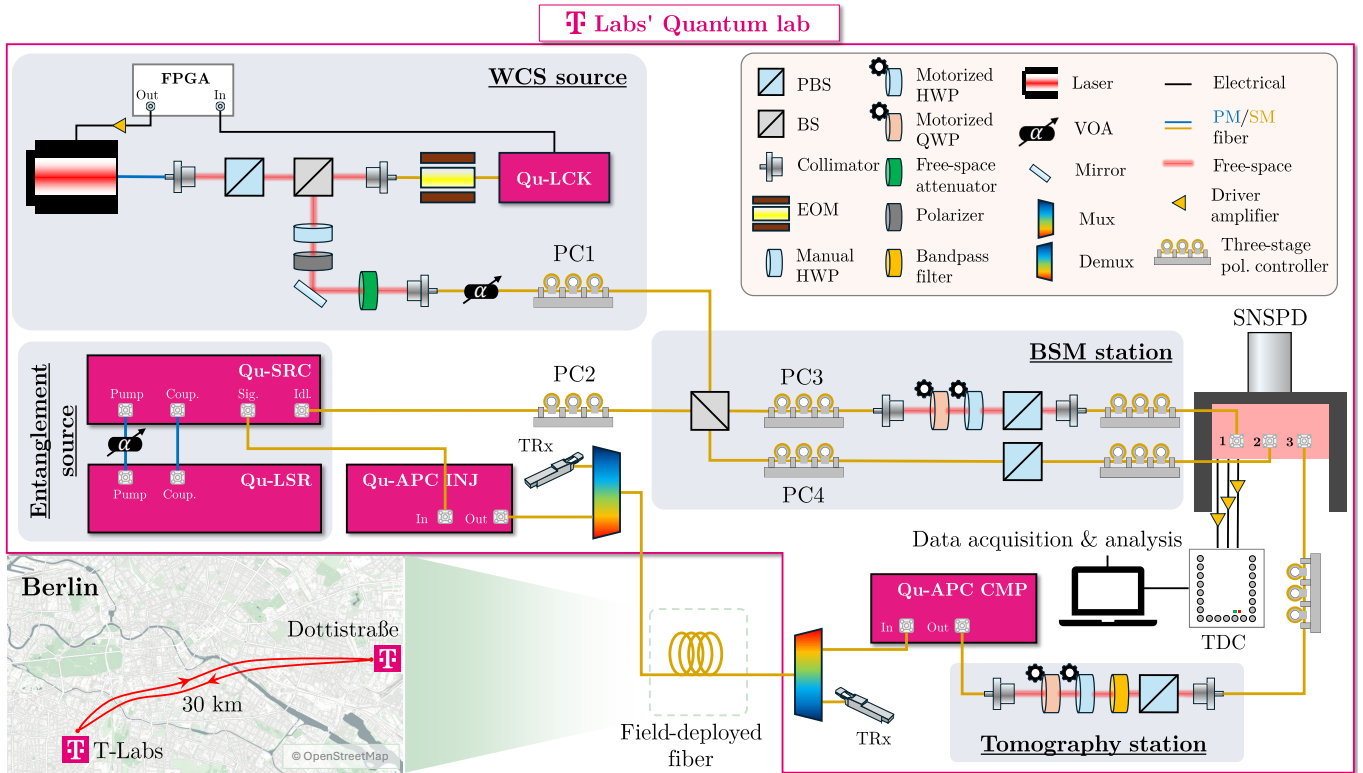


FIG. 1. Schematic of the field-deployed teleportation experiment on Deutsche Telekom’s R&D fiber test network in Berlin. A 795-nm weak coherent state (WCS) interferes with the 795-nm idler photon of a bichromatic polarization-entangled pair at a local Bell-state measurement (BSM). Conditional on a successful BSM, the input polarization state is transferred, up to a known unitary, onto the 1324-nm signal photon, which is transmitted over a 30-km deployed fiber and analyzed by polarization tomography. Co-propagating C-band classical traffic is multiplexed onto the same fiber as indicated.

device-to-telecom state-transfer interface under carrier-grade metropolitan conditions.

In this work, we present the preliminary results of a field trial conducted on Deutsche Telekom’s R&D fiber test network in Berlin. A polarization-encoded input qubit at low near-infrared (NIR) wavelength, prepared using a weak coherent source, interferes with another low-NIR photon from a bichromatic entangled pair; a successful Bell-state measurement teleports the input state onto the local telecom-band partner photon, which is subsequently transmitted over the deployed fiber network. Measurements are performed in both a dark-fiber configuration and in the presence of co-propagating classical traffic of a 10 Gbit/s dense wavelength-division multiplexing (DWDM) signal in the C-Band.

II. EXPERIMENTAL SETUP

In this section, we detail each of the main components of the experimental setup illustrated in Figure 1.

A. Weak Coherent State Source

The input polarization states to be teleported are prepared by an attenuated continuous-wave (CW), frequency-locked, 795 nm DBR laser. For locking, the laser light is phase-modulated with an electro-optical modulator (EOM) and sent to a rubidium (Rb) spectroscopy module (Qu-LCK) containing a warm ^{87}Rb vapor cell. The absorption signal is processed by an FPGA to derive an error signal. The locking position is chosen such that the laser’s wavelength is well overlapped with the emission profile of the Qu-SRC idler photons.

The laser light is coarsely attenuated with neutral density filters and further fine-tuned with a fiber-based voltage-controlled variable optical attenuator (VOA) to reach the single photon level while maintaining control over the single photon rate. Finally, a motorized three-stage polarization controller (PC1) prepares the input polarization state for teleportation.

Throughout the experiment, the WCS operates in the single photon regime at the BSM. This configuration provides a simple, tunable, and field-deployable transmitter for the commissioning and benchmarking of teleportation interfaces. At the same time, the residual multi-photon component constitutes a realistic impairment that is di-

rectly reflected in the measured HOM visibility and the resulting teleportation fidelities [13].

For the local fiber configuration, the detected rates on channel 1 and 2 for the WCS are ~ 2.6 Mcps and ~ 5.6 Mcps. The transmission efficiency from BS to the detector is $\sim 2.5\%$ for channel 1 and $\sim 5\%$ for channel 2.

B. Bright Polarization Entanglement Source

We generate polarization-entangled photon pairs using Qunnect's Qu-SRC. This bichromatic source generates non-degenerate photon pairs at 795 nm (idler) and 1324 nm (signal) from a warm ^{87}Rb ensemble via spontaneous four-wave mixing in a diamond configuration [14]. The pump and coupling fields are generated by the Qu-LSR laser system and delivered via polarization-maintaining (PM) fiber, with a VOA in the pump path to tune the source pair rate. The emitted state approximates $|\Phi^+\rangle = (|HH\rangle + |VV\rangle)/\sqrt{2}$ with 95% fidelity. Its wavelength asymmetry supports hybrid networking: 1324 nm enables low-loss telecom transmission, while 795 nm is compatible with Rb-based quantum devices. At the source output, 795 nm idler photons pass through a motorized polarization controller (PC2) before the BSM station, while 1324 nm signal photons are routed through metro fibers.

For the local fiber configuration, the detected idler photon rates on channels 1 and 2 are ~ 100 kcps and ~ 240 kcps. The detected signal photon rate on channel 3 is ~ 200 kcps. Given a 64 ps window, the detected coincidence rate between channels 2 and 3 is ~ 1.6 kcps (coincidences between channels 1 and 3 are proportional to the difference in loss).

C. Bell State Measurement Station

The WCS photon carrying the state to be teleported and the 795 nm idler photon generated by the Qu-SRC are sent to a local Bell-state measurement (BSM) station. The photons interfere at a fiber-based 2×2 non-polarizing 50 : 50 BS, whose outputs are connected to motorized polarization controllers (PC3 in the upper path and PC4 in the lower path, Figure 1). In the upper path, photons pass through a free-space motorized QWP, motorized HWP, and a free-space PBS; in the lower path, they pass through a fiber-based PBS only. The PBS outputs from the upper and lower paths are routed to channels 1 and 2 of the Single Quantum Superconducting Nanowire Single-Photon Detectors (SNSPDs) system, respectively. The SNSPD channel detection efficiencies are $\sim 82\%$, $\sim 90\%$, and $\sim 92\%$ for channels 1, 2, and 3 respectively (with jitter ~ 20 ps). Electrical signals from single-photon detections are time-tagged using a Swabian Instruments time-to-digital converter (TDC), and the resulting timestamps are processed by a data acquisition and analysis computer.

D. Field-Deployed Fiber Loop and Stabilization

We characterize the field-deployed fiber with an optical time-domain reflectometer (OTDR), as real-world fibers exhibit imperfections including splice and coupler losses, as well as additional attenuation from manufacturing or installation inconsistencies. The selected loop between T-Labs' Quantum Lab and Deutsche Telekom's office on Dottistraße shows losses close to expected values. The measured attenuation profile closely matches that of the standard single-mode fiber (SMF) at 1324 nm, as indicated by the red curve in Figure 2.

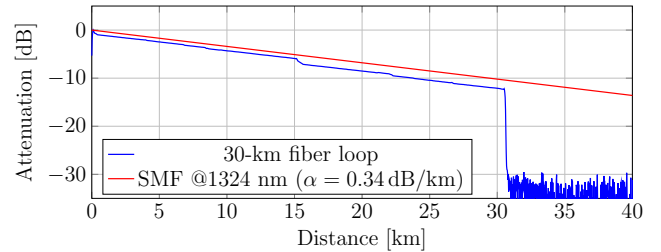


FIG. 2. OTDR trace of the 30-km deployed fiber loop used in this experiment (T-Labs to Dottistraße). Discontinuities correspond to connectors, splices, or patch-panel events. The red line indicates the expected attenuation of standard SMF at 1324 nm (approximately 0.34 dB/km).

To ensure stable operation over the fiber, we employ Qu-APC to compensate for fiber-induced polarization rotations [10, 15]. The Qu-APC modules can be activated at predefined intervals during long acquisitions, maintaining stable polarization throughout the 30-km loop despite gradual drift [7]. Beyond active drift compensation, it also enables a calibration strategy that circumvents loss-induced limitations. Direct polarization calibration across the full deployed span is restricted by accumulated attenuation and a reduced signal-to-noise ratio (SNR). Calibration is performed locally on a short fiber with a high SNR and then switched to the 30 km field-deployed link, while the modules automatically compensate for the new fiber transformation. This procedure enables reliable polarization calibration independent of link length and supports dynamic fiber reconfiguration via optical switches [8]. In the present configuration, the total end-to-end attenuation from the output of Qu-APC INJ to the input of Qu-APC CMP is 18 dB, including deployed fiber loss, Mux/Demux insertion loss, and connector and patch-panel losses.

Due to the loss of the 30 km fiber, the pump power to the Qu-SRC was increased to overcome attenuation; however, this also required adjusting the WCS rate to account for this change. After increasing the pump power to the Qu-SRC, the detected single photon rates on channels 1, 2, and 3 are ~ 350 kcps, ~ 780 kcps, and ~ 34 kcps respectively with a coincidence rate of 300 cps measured between channels 2 and 3. Leakage from the classical co-propagating light amounted to an addition of ~ 51 kcps

of uncorrelated noise to channel 3. The detected rate of the WCS for this case is ~ 10 Mcps.

E. State Tomography Analysis Station

After exiting the Qu-APC INJ at T-Labs, the signal photons are multiplexed (Mux, Figure 1), transmitted through the field-deployed fiber loop, returned to the lab, demultiplexed (Demux, Figure 1), routed through the Qu-APC CMP, and delivered to the tomography station. The Mux/Demux is necessary to combine/separate the O- and C-band signals, i.e., the single photons and the co-propagating classical traffic, respectively. The tomography station features fiber-coupled input and output interfaces with free-space, motorized polarization analysis. Projective measurements in the selected polarization bases are implemented using QWP, HWP, and PBS. At the output, a manual polarization controller aligns the state to the preferred SNSPD axis, and detection events are time-tagged with the TDC.

III. QUANTUM TELEPORTATION

We demonstrate quantum state teleportation of three representative polarization states, $\{|H\rangle, |D\rangle, |R\rangle\}$ under two different conditions: Locally (within the T-labs) and over the deployed network. The reported fidelities correspond to conditional state-transfer events heralded by a successful BSM and detection of the associated signal photon. The upper-bound of the fidelity of the teleported state can be estimated by the indistinguishability of the two interfering photons and can be inferred from the HOM visibility. We measure the HOM visibility both locally (bypassing the 30km fiber) and through the deployed network (without classical traffic). HOM interference measured in the local fiber configuration, bypassing the field-deployed span, yields a visibility of $V = 72.8 \pm 5.3\%$. The 30 km deployed-fiber network resulted in a visibility of $V = 68.6 \pm 5.6\%$. The reduced visibility in the 30 km configuration is attributed to the higher rate operating point required to compensate for the additional link loss. At higher brightness, the effective single-photon quality of the entangled-photon source degrades, which lowers the measured HOM visibility.

It is important to note that for each PBS, only one output port is monitored (i.e. the transmitted port rather than the reflected one). Consequently, we are restricted to measuring three-fold coincidences conditioned exclusively on the $|\Psi^-\rangle$ BSM outcome.

At the tomography station, the QWP and HWP are rotated to six different configurations to measure three-fold coincidences in the six bases.

These measurement settings are used to reconstruct the density matrix ρ of the teleported state through the nor-

State	QWP (°)	HWP (°)
$ H\rangle$	0	0
$ V\rangle$	0	45
$ D\rangle$	45	22.5
$ A\rangle$	45	67.5
$ R\rangle$	45	0
$ L\rangle$	0	22.5

TABLE I. QWP and HWP rotation angles used in the tomography station to project onto the polarization basis states $\{|H\rangle, |V\rangle, |D\rangle, |A\rangle, |R\rangle, |L\rangle\}$.

malized Stokes parameters S_x , S_y , and S_z ,

$$\rho = \frac{1}{2} \left(I + S_x \sigma_x + S_y \sigma_y + S_z \sigma_z \right), \quad (1)$$

where I denotes the identity operator and σ_i ($i = x, y, z$) are the Pauli matrices. The Stokes parameters are obtained from the measured threefold coincidence counts C in the corresponding polarization bases as:

$$(S_x \ S_y \ S_z) = \left(\frac{C_D - C_A}{C_D + C_A} \ \frac{C_R - C_L}{C_R + C_L} \ \frac{C_H - C_V}{C_H + C_V} \right). \quad (2)$$

The fidelity F of the teleported state with respect to the target state is then evaluated as follows:

$$F = \langle \psi_T | \rho | \psi_T \rangle, \quad (3)$$

where $|\psi_T\rangle$ denotes the target polarization state. Table II provides the correspondence between the teleported state and the consequently received state given the BSM detection conditioned on $|\Psi^-\rangle$, for the three states used to demonstrate quantum teleportation. For statistical purposes and better error estimation, data were taken over 60 seconds for local teleportation datasets and over 180-600 seconds (per waveplate setting) for 30-km datasets.

Teleported	Received ($ \Psi^-\rangle$)
$ H\rangle$	$ V\rangle$
$ D\rangle$	$ A\rangle$
$ R\rangle$	$ R\rangle$

TABLE II. State mapping conditioned on the $|\Psi^-\rangle$ Bell-state measurement outcome. No corrective unitary is applied.

We report single-state tomography reconstructions (Figure 3, Figure 4) for local and field-deployed demonstrations. For each teleported state, the reconstructed density matrix is displayed as real (left) and imaginary (right) components, with positive (negative) matrix elements shown in magenta (blue). The output states displayed $\{|V\rangle, |A\rangle, |R\rangle\}$ are obtained from the corresponding input states $\{|H\rangle, |D\rangle, |R\rangle\}$, consistent with the expected state mapping in the absence of the unitary correction. We demonstrate an average fidelity of $92.3 \pm 2.2\%$ for the local experiment and $90.1 \pm 3.3\%$ after 30 km of deployed fiber propagation. The decrease in fidelity can be directly attributed to the decrease in the HOM visibility.

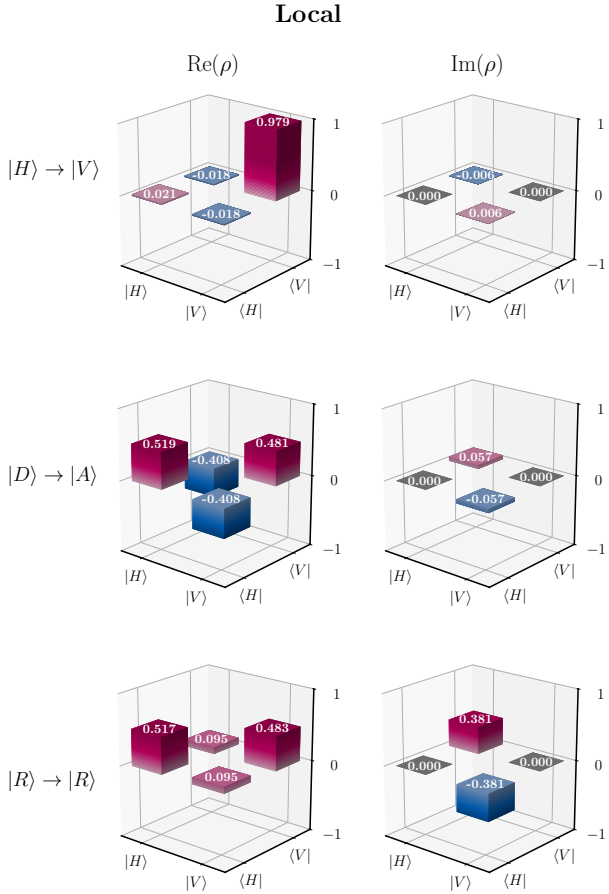


FIG. 3. Reconstructed density matrices ρ (real and imaginary parts) from single-state tomography for local teleportation. Matrix elements are shown in the $\{|H\rangle, |V\rangle\}$ basis. Positive (negative) values are shown in magenta (blue).

IV. QUANTUM TELEPORTATION WITH CO-PROPAGATING CLASSICAL DATA

Quantum teleportation over the fiber loop with co-propagating classical and quantum signals is performed using the same measurement protocol, demonstrating successful operation in the presence of co-propagating classical traffic. A pair of optical transceivers (TRx) is directly connected to Mux and Demux in the setup (see Figure 1). The classical channel is provided by an ADVA 10G DWDM centered at 1561.42 nm and operated at a fixed output power of 1 dBm. A 12-nm bandpass filter is inserted between the HWP and PBS at the tomography station to partially suppress spurious light on channel 3.

The single-state tomography results for this experiment are shown in Figure 5. Compared to operation without classical traffic, the fidelity decreases from $90.1 \pm 3.3\%$ to $85.9 \pm 4.3\%$, consistent with the residual crosstalk of the classical band reaching the detectors despite additional bandpass filtering.

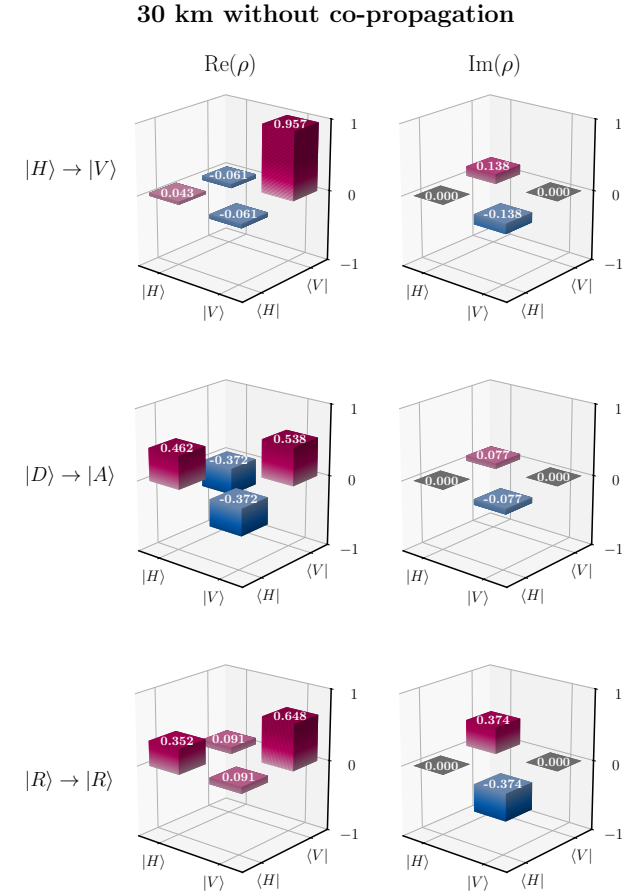


FIG. 4. Density matrices from single-state tomography for the 30-km deployed-fiber configuration without co-propagating classical light. Matrix elements are shown in the $\{|H\rangle, |V\rangle\}$ basis. Positive (negative) values are shown in magenta (blue).

The corresponding fidelities of all three received states $\{|V\rangle, |A\rangle, |R\rangle\}$ are shown in Figure 6 by the magenta and blue bars. Using the average of all target states, the fidelities exceed the classical limit depicted by the dashed line, with the 30-km configuration reaching an average value of approximately $90.1 \pm 3.3\%$. The fidelity uncertainty was estimated using a Monte Carlo simulation. Threefold coincidence counts were sampled from a Poissonian distribution [16], and the fidelity calculation was repeated for 10,000 trials to determine the standard deviation of the fidelity distribution.

Beyond proof-of-principle state transfer, this measurement serves as a system-level diagnostic of the full teleportation chain, including photon indistinguishability at the BSM, polarization-transport stability with compensation, and robustness to background light and co-propagating classical traffic. Thus, a tunable WCS input enables repeatable injection of known test states to characterize hybrid quantum-classical network nodes and quantify conditional quantum correlations preserved through a deployed channel.

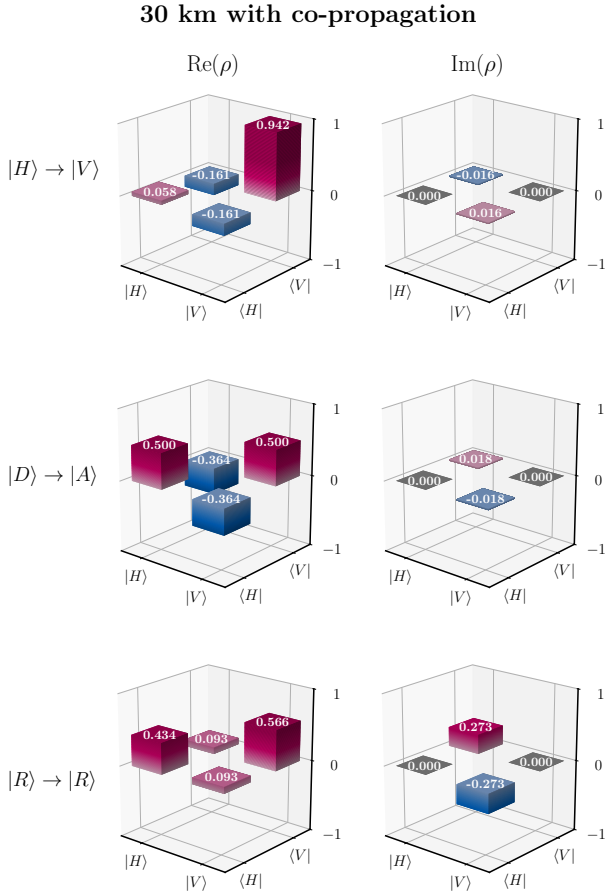


FIG. 5. Reconstructed density matrices ρ (real and imaginary parts) from single-state tomography for the 30-km deployed-fiber configuration with co-propagating classical traffic. Matrix elements are shown in the $\{|H\rangle, |V\rangle\}$ basis. Positive (negative) values are shown in magenta (blue).

V. CONCLUSION

We demonstrate quantum teleportation over Deutsche Telekom’s carrier-grade metropolitan fiber network in Berlin using commercially available, field-deployable components. A local Bell-state measurement between 795 nm photons from a weak coherent source and from a bichromatic warm-atom entangled-photon source enabled conditional state transfer onto a telecom O-band photon. The teleported photon was then transmitted through a 30-km field-deployed fiber loop under real-world environmental perturbations and, optionally, with co-propagating C-band classical data traffic. Teleporting the input states $\{|H\rangle, |D\rangle, |R\rangle\}$ yielded the expected outputs $\{|V\rangle, |A\rangle, |R\rangle\}$. Averaged over the three inputs, the fidelities were $90.1 \pm 3.3\%$ without co-propagating traffic and $85.9 \pm 4.3\%$ with traffic. Although based on weak coherent inputs, the post-selected $|\Psi^-\rangle$ results establish a deployable method to benchmark hybrid

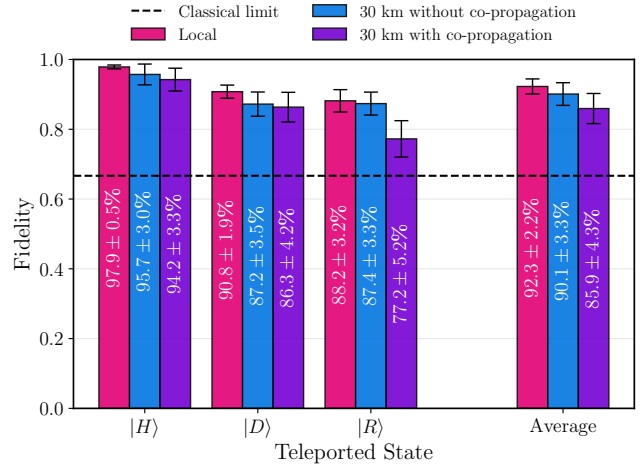


FIG. 6. Teleportation fidelities for the prepared input states $\{|H\rangle, |D\rangle, |R\rangle\}$, corresponding (for $|\Psi^-\rangle$) conditioning and without feed-forward to received target states $\{|V\rangle, |A\rangle, |R\rangle\}$. Results are shown for local, 30 km deployed fiber without co-propagation, and 30 km with co-propagating classical traffic. Rightmost bars show the average fidelity for all configurations. The black dashed line indicates the classical measure-and-prepare bound $F = 2/3$. The uncertainties are estimated using a Monte Carlo simulation. Variations in the uncertainties are due to the difference in rates between the local and 30 km fiber configurations as well as measurement duration.

quantum-classical nodes in existing infrastructure. The measurements quantify polarization drift and classical-channel crosstalk under carrier-grade conditions and represent a practical step toward scalable metro-scale quantum networks employing teleportation-based protocols. Furthermore, from a network-architecture perspective, this work also targets the end-node state-transfer interface that complements telecom-band primitives such as entanglement distribution [11] and entanglement swapping [12]. The bichromatic teleportation bridges device-compatible photons at 780–795 nm, relevant for Rb-based processors, memories, clocks, and sensors, to telecom photons suitable for metro-scale fiber transport.

VI. ACKNOWLEDGMENTS

The authors acknowledge partial financial support from the German Federal Ministry of Research, Technology and Space (BMFTR) under the project *QR.N* (FKZ 16KIS2181).

[1] C. H. Bennett, G. Brassard, C. Crépeau, R. Jozsa, A. Peres, and W. K. Wootters, Teleporting an unknown quantum state via dual classical and einstein-podolsky-rosen channels, *Phys. Rev. Lett.* **70**, 1895 (1993).

[2] H. J. Kimble, The quantum internet, *Nature* **453**, 1023 (2008).

[3] D. Main, P. Drmota, D. P. Nadlinger, E. M. Ainley, A. Agrawal, B. C. Nichol, R. Srinivas, G. Araneda, and D. M. Lucas, Distributed quantum computing across an optical network link, *Nature* **638**, 383 (2025).

[4] H. R. Jahromi, Remote sensing and faithful quantum teleportation through non-localized qubits, *Physics Letters A* **424**, 127850 (2022).

[5] H.-J. Briegel, W. Dür, J. I. Cirac, and P. Zoller, Quantum repeaters: The role of imperfect local operations in quantum communication, *Phys. Rev. Lett.* **81**, 5932 (1998).

[6] J. M. Thomas, F. I. Yeh, J. H. Chen, J. J. Mambretti, S. J. Kohlert, G. S. Kanter, and P. Kumar, Quantum teleportation coexisting with classical communications in optical fiber, *Optica* **11**, 1700 (2024).

[7] M. Sena, M. Flament, M. Namazi, S. Andrewski, G. Portmann, R.-P. Braun, M. Youssef-Sayed, R. Döring, M. Ritter, O. Holschke, and M. Geitz, High-fidelity entanglement distribution through berlin using an operator's fiber infrastructure, in *Optical Fiber Communication Conference (OFC) 2025* (Optica Publishing Group, 2025) p. M4E.2.

[8] T. Rieser, M. Sena, S. Andrewski, N. Bigagli, M. Flament, R.-P. Braun, M. Ritter, M. Namazi, and M. Geitz, Distributing, routing and multiplexing o-band polarization-entangled photons with c-band classical light over an operator's metropolitan fiber network, in *Proceedings of the European Conference on Optical Communication (ECOC)* (Copenhagen, Denmark, 2025).

[9] Y.-R. Fan, Y. Luo, Z.-C. Zhang, Y.-B. Li, S. Liu, D. Wang, D.-C. Zhang, G.-W. Deng, Y. Wang, H.-Z. Song, Z. Wang, L.-X. You, C.-Z. Yuan, G.-C. Guo, and Q. Zhou, Energy-time entanglement coexisting with fiber-optical communication in the telecom *c* band, *Phys. Rev. A* **108**, L020601 (2023).

[10] A. N. Craddock, A. Lazenby, G. B. Portmann, R. Sekelsky, M. Flament, and M. Namazi, Automated distribution of polarization-entangled photons using deployed new york city fibers, *PRX Quantum* **5**, 030330 (2024).

[11] M. Sena, M. Flament, S. Andrewski, I. Caltzidis, N. Bigagli, T. Rieser, G. B. Portmann, R. Sekelsky, R.-P. Braun, A. N. Craddock, M. Schulz, K. D. Jöns, M. Ritter, M. Geitz, O. Holschke, and M. Namazi, High-fidelity quantum entanglement distribution in metropolitan fiber networks with co-propagating classical traffic, *J. Opt. Commun. Netw.* **17**, 1072 (2025).

[12] A. N. Craddock, T. Cowan, N. Bigagli, S. Yekasiri, D. Robinson, G. B. Portmann, Z. Guo, M. Kilzer, J. Zhao, M. Flament, J. Shabani, R. Nejabati, and M. Namazi, High-rate scalable entanglement swapping between remote entanglement sources on deployed new york city fibers (2026), submitted 17 Feb 2026, arXiv:2602.15653.

[13] A. Xu, L. Duan, L. Wang, and Y. Zhang, Characterization of two-photon interference between a weak coherent state and a heralded single photon state, *Opt. Express* **31**, 5662 (2023).

[14] A. N. Craddock, Y. Wang, F. Giraldo, R. Sekelsky, M. Flament, and M. Namazi, High-rate subgigahertz-linewidth bichromatic entanglement source for quantum networking, *Phys. Rev. Appl.* **21**, 034012 (2024).

[15] M. Flament, M. Namazi, G. B. Portmann, and R. Sekelsky, Systems and methods for real-time polarization drift compensation in optical fiber channels used for quantum communications, Patent US12361308B2 (2025), available: <https://patents.google.com/patent/US12361308B2/>.

[16] D. F. V. James, P. G. Kwiat, W. J. Munro, and A. G. White, Measurement of qubits, *Phys. Rev. A* **64**, 052312 (2001).